ADVANCED FUNCTIONAL MATERIALS
www.afm-journal.de



# Implementing Thermometry on Silicon Surfaces Functionalized by Lanthanide-Doped Self-Assembled Polymer Monolayers

*Mafalda Rodrigues, Rafael Piñol, Guillermo Antorrena, Carlos D. S. Brites, Nuno J. O. Silva, José Luis Murillo, Rafael Cases, Isabel Díez, Fernando Palacio, Núria Torras, José Antonio Plaza, Lluïsa Pérez-García, Luís D. Carlos,* and Angel Millán**

**The thermal gradients generated at submicrometer scale by the millions of transistors contained in integrated circuits are becoming the key limiting factor for device integration in micro- and nanoelectronics. Noncontact thermometric techniques with high-spatial resolution are, thus, essential for noninvasive off-chip characterization and heat management on Si surfaces. Here, the first ratiometric luminescent molecular thermometer implemented in a self-assembled polymer monolayer functionalized Si surface is reported. The functionalization of Si surfaces with luminescent thermometers constitutes a proof-of-concept that foretells a wide range of applications in Si-based micro- and nanostructures. The thermometric functionalization of the Si surface with $Tb^{3+}$ and $Eu^{3+}$ complexes leads to a thermal sensitivity up to 1.43% $K^{-1}$, a cycle–recycle reliability of 98.6%, and a temperature uncertainty of less than 0.3 K. The functionalized surface presents reversible bistability that can be used as an optically active molecular demultiplexer.**

## 1. Introduction

Surface functionalization (particularly semiconductor surfaces) through direct molecule attachment is a recurrent way for endorsing a substrate with additional properties, allowing the tailoring of the surface's chemical, physical, and electronic properties.[1–4] The integration of the functionalities of organic molecules into semiconductor-based materials and devices has a substantial impact on numerous applications, such as micro and optoelectronics, microelectromechanical machines, memory chips, Si-based biological sensors, and in the development of microelectronic computing.[5] Among the wide scope of possible surface functionalities, thermometry is probably the most useful, due to its high relevance to societal needs. Temperature measurements are crucial in countless technological and industrial developments and in scientific research, accounting actually for ≈80% of the sensor market throughout the world (the global market is likely to grow to $6.13 billion in 2020).[6] Moreover, among the possible substrates silicon is, by far, the most important material for semiconductor devices and integrated circuits manufacturing.[7,8] The thermal gradients generated at submicrometer scale by the millions of transistors incorporated in modern semiconductor devices (e.g., microprocessors) makes thermometric techniques with high-spatial resolution critical in micro- and nanoelectronics, particularly in noninvasive off-chip characterization and heat management.[9–11]

There are many examples of functionalized Si-based surfaces, usually with the purpose to develop chip-based chemical or biological sensors.[2,12] However, to the best of our knowledge, there are no precedents in the literature of Si-coating

Dr. M Rodrigues, Dr. L. Pérez-García
Department de Farmacologia i Química Terapèutica and Institut de Nanociència i Nanotecnologia UB (IN2UB)
Universitat de Barcelona
Avda. Joan XXIII s/n
08028 Barcelona, Spain

Dr. R. Piñol, Dr. J. L. Murillo, Dr. R. Cases, Dr. I. Díez, Prof. Dr. F. Palacio, Dr. A. Millán
Departamento de Física de la Materia Condensada
Facultad de Ciencias and Instituto de Ciencia de Materiales de Aragón
CSIC-Universidad de Zaragoza
50009 Zaragoza, Spain
E-mail: amillan@unizar.es

DOI: 10.1002/adfm.201503889

Dr. G. Antorrena
Laboratorio de Microscopías Avanzadas (LMA)
Instituto de Nanociencia de Aragón (INA)
Universidad de Zaragoza
Edificio I+D
C./Mariano Esquillor s/n. 50018 Zaragoza, Spain

Dr. C. D. S. Brites, Dr. N. J. O. Silva, Prof. Dr. L. D. Carlos
Departamento de Física and CICECO-Aveiro Institute of Materials
Universidade de Aveiro
3810-193 Aveiro, Portugal
E-mail: lcarlos@ua.pt

Dr. N. Torras, Dr. J. A. Plaza
Instituto de Microelectrónica de Barcelona
IMB-CNM (CSIC)
Campus UAB
08193 Bellaterra, Barcelona, Spain

layers permitting the determination of the temperature near the physiological range with submicrometer and subdegree resolution, and, thus, it is worthy to develop thermometric coatings for silicon-based devices (especially biochips).[13] Although IR cameras are commonly used in thermometry, they present the following disadvantages: i) limited spatial resolution (>100 μm); ii) previous knowledge of the material surface emissivity (that is function of wavelength and temperature); iii) considerable temperature uncertainty (≈2° at room temperature, acceptable values only above 318 K), and iv) strong dependence on the relative orientation between the camera and the measured surface.[14,15] Moreover, sometimes it is difficult to measure the emissivity of metal layers precluding an appropriate temperature estimation.[16] Covering layers for emissivity correction can distort the thermal field and could be incompatible with the inspected sample.

The wisest solution should combine the advantages of noncontact measurements, even in biological fluids and in the presence of strong electromagnetic fields, with high spatial and temperature resolutions. One of the most promising techniques is luminescent thermometry that uses the photoluminescence of semi-invasive probes to determine the temperature based on changes on the emission intensity, peak position, band shape, decay time, or rise time.[17–19] Temperature measurements based on intensity changes demand ratiometric (or self-referencing) readout. The intensity ratio between two transitions is not compromised by the well-known disadvantages of experiments based on the intensity of only one transition, such as the critical dependence on variations of the sensor concentration, small material inhomogeneities and optoelectronic drifts of the excitation source and detectors, and, thus, are much more reliable.[17–19]

The most available and used luminescent probes are based on organic dyes;[20] however, quantum dots[21] are gaining relevance due to the higher photostability and relatively high emission quantum yields. Quantum dots are often formed by highly cytotoxic elements (e.g., Cd) which difficult its future use on clinical trials.[22,23] Lanthanide-based materials, however, are versatile, stable, and narrow band emitters with, in general, high emission quantum yields (>50%).[24] In fact, different emitting centers can cover the entire electromagnetic spectrum, ranging from the ultraviolet (e.g., $Gd^{3+}$) to the IR (e.g., $Er^{3+}$, $Yb^{3+}$, $Nd^{3+}$), thus it is virtually possible to design on-demand luminescent probes for a large variety of applications.[25] In the literature, we can find numerous examples of temperature measurements using lanthanide-based molecular thermometers covering temperatures from the cryogenic to the physiological range.[26–33] These probes are especially attractive as they can be processed as thin or thick films, monoliths or nanoparticles, enabling the ratiometric temperature determination with reported uncertainty in the 0.01 K range.[26,34,35]

Here we report, to the best of our knowledge, the first ratiometric luminescent molecular thermometer implemented in a self-assembled monolayer (SAM) of polymer functionalized Si surface. The functionalization of Si surfaces with luminescent thermometers constitutes a proof-of-concept that foretells a wide range of applications in Si-based micro and nanostructures. The thermometric functionalization of the Si surface with $Tb^{3+}$ and $Eu^{3+}$ complexes lead to a sensitivity up to 1.45% $K^{-1}$, cycle–recycle reliability of 98.6%, and temperature uncertainty less to 0.3 K. Moreover, the system presents reversible bistability opening a new route for study optically active double-input molecular logical gates using the excitation wavelength and the heat transferred to (or from) the system as inputs and the dependence on temperature of the thermometric parameter as output.

## 2. Results

### 2.1. Producing Self-Assembled Monolayers Functionalized with Lanthanide β-Ketoester Complexes on a Si Surface

Synthesis of precursors is detailed in Section 1 of the Supporting Information. Silicon wafers with three different surface coating materials were used for thermometric SAM coating: i) monocrystalline Si, ii) $SiO_2$ deposited by plasma-enhanced chemical vapor deposition (PECVD), and iii) polycrystalline Si deposited by low-pressure chemical vapor deposition. The production of functionalized Si surfaces is detailed in Section 2 of the Supporting Information. The thermometric coating is performed in several steps as shown schematically in **Figure 1**a. Previously cleaned surfaces were activated by treatment with a piranha solution (wet method)[36] or UV/ozone (dry method) generating surface silanol groups, with similar results (Supplementary Information). Then, the activated substrate was reacted with APTES by vapor deposition at low pressure and the acetoacetyl polyethylenglycol acrylate (acacPEGA) polymer is attached to the amine-modified surface by a Michael addition of the acrylate onto the amine surface groups. This addition benefits from mild reaction conditions, high functional groups tolerance, no by-products, as well as high conversion and favorable reaction rates.[36] Finally, lanthanide coordination compounds are formed with the keto-ester moieties at the end of the acacPEGA polymer and the DPA ligands (Figure 1b). The DPA ligand is selected as it is one of the most effective sensitizers of $Eu^{3+}$ and $Tb^{3+}$ luminescence,[37] but β-diketone ligands[38] will also work.

### 2.2. Characterizing the Self-Assembled Monolayers

Several experiments were performed to characterize the functionalization process (Section 3 in the Supporting Information). The wettability of the surfaces was analyzed using contact angle measurements. Both wet and dry activation processes resulted in a good surface wettability indicated by the measured contact angles: 46°, 67°, and 70° for $SiO_2$, polycrystalline Si, and monocrystalline Si, respectively. After APTES deposition, contact angles increased for all surfaces to values between 91° and 95°. Then, after the Michael reaction, the contact angles decreased to values around 45° and 56° reflecting the highly hydrophilic character of the PEG chains (Table S5 in the Supporting Information).

On the other hand, AFM results (**Figure 2**a; Tables S1–S4 and Figure S1 in the Supporting Information) show no significant changes in roughness after APTES coating, independently of the substrate or the activation method, and island formations

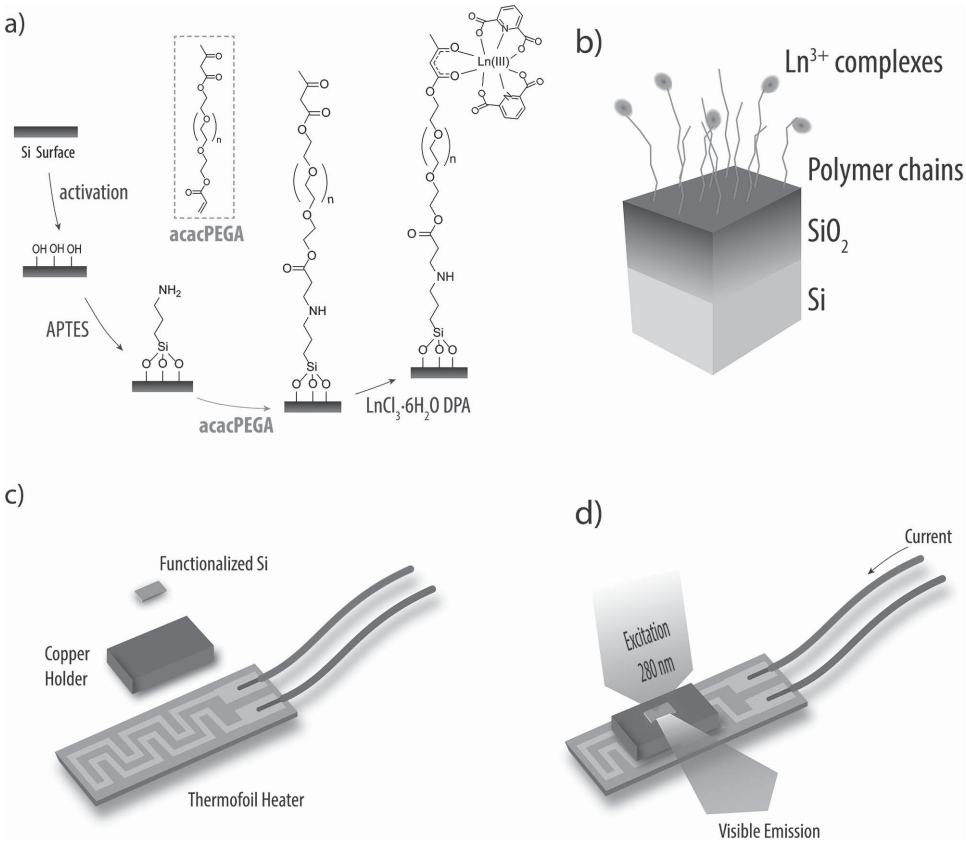


**Figure 1.** a) Schematic of the Si surface functionalization with thermometric SAM showing the activation step, the functionalization with APTES, the reaction with the PEGA polymer (structure in inset) and the formation of the $Eu^{3+}$ and $Tb^{3+}$ complexes. b) Schematic of the Si-functionalized surface incorporating the temperature responsive $Ln^{3+}$ complexes. c) Exploded view of the setup used for the thermometric characterization of the sample, showing the thermofoil heater, the copper holder, and the Si-functionalized surface. d) Schematic of the setup under 280 nm excitation that emits in the visible.

are not discerned, contrarily to what is frequently founded in solution coatings.[39]

A detailed account of XPS analysis along the whole functionalization process is given in Section 4 in the Supporting Information. Analysis of surfaces after wet or dry activation shows the presence of $Si^0$ and $SiO_2$ (Figure 2b; Table S2 in the Supporting Information). The spectra of the samples after APTES deposition clearly display the N 1s peak (Figure 2c; Table S2 in the Supporting Information). The estimated C:N ratio (C:N = 9), is higher than that corresponding to a fully polymerized APTES (C:N = 3), indicating, probably, the incomplete hydrolysis of lateral alkoxides groups. The ratio of free ($NH_2$) to protonated ($NH_3^+$) amines was estimated to 0.535, from the intensity of peaks at 399.7 and 401.6 eV, respectively.[40] XPS of surfaces after reaction with acacPEGA (Figure 2d) show C 1s spectrum that can be deconvoluted into four main peaks, at 284.9 eV (C–C, calibration), +1.6(2) eV, +3.2(2) eV, and +4.2(2) eV, that correspond to the four oxidation states of C in acacPEGA structure. The incorporation of $Tb^{3+}$ and $Eu^{3+}$ ions into the coating was also confirmed by XPS that showed also the presence of both ions after the anchoring of the lanthanide $\beta$-ketoester complexes (Figure 2e,f). A Tb:Eu molar ratio of 2.7 was estimated from the Tb 3d and Eu 3d spectra, which is close to the nominal one (Tb:Eu = 3).

### 2.3. Temperature-Dependent Photoluminescence

The sample with a $SiO_2$ surface deposited by PECVD, activated with plasma, coated with APTES by vapor deposition and with acacPEGA in water and, then, functionalized with the Ln-DPA (Ln = Eu, Tb) complexes was selected to perform the thermometric characterization (**Figure 3**). The experimental setup is shown in Figure 1c,d.

The room temperature excitation spectra recorded monitoring the $^5D_4 \rightarrow {}^7F_5$ ($Tb^{3+}$) and the $^5D_0 \rightarrow {}^7F_2$ ($Eu^{3+}$) transitions are dominated by an intense broad band (260–390 nm) ascribed to the DPA excited singlet states.[37,41] Indeed, in this wavelength range the two excitation spectra are identical to that reported for free DPA,[37,41] including the carbonyl fine structure (more evident in the spectrum monitored in the $Tb^{3+}$ transition). There is no evidence of $Tb^{3+}$-to-$Eu^{3+}$ energy transfer since no intra-$4f^8$ lines are discerned in the excitation spectrum monitored on the $^5D_0 \rightarrow {}^7F_2$ transition (for instance the $^7F_6 \rightarrow {}^5D_4$ line at ≈477 nm). This is in good agreement with the structural model depicted in Figure 1a in which the $Tb^{3+}$ and $Eu^{3+}$ coordination sites in the functionalized Si surface are well apart making $Tb^{3+}$-to-$Eu^{3+}$ energy transfer highly improbable (there is one $Tb^{3+}$ or $Eu^{3+}$ coordinated acacPEGA chain per 6 uncoordinated ones and the $Tb^{3+}$: $Eu^{3+}$ ratio is 3:1, Supporting Information).

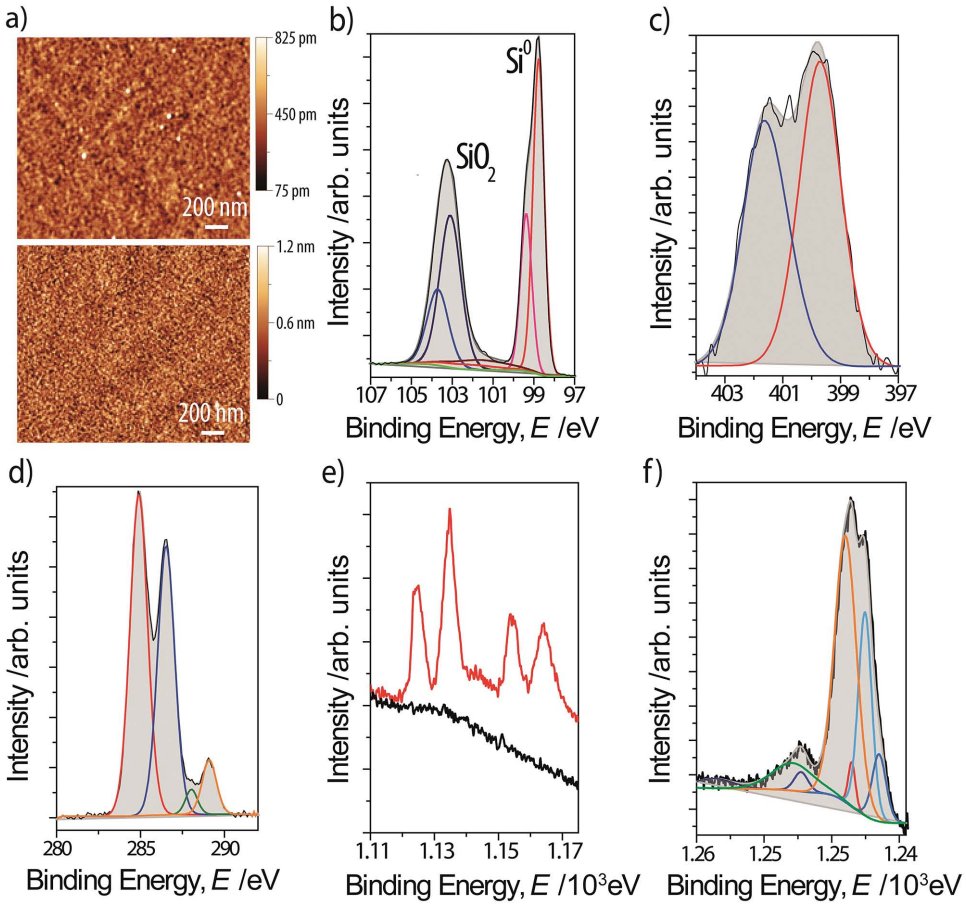


**Figure 2.** a) AFM images of monocrystalline Si surfaces before (top) and after (bottom) APTES deposition. b) XPS spectrum of polycrystalline Si wafers. The Si 2p signal of an oxidized wafer (black) and the peak components (colored solid lines) are presented, as well as the $SiO_2$ (103 eV) and bulk $Si^0$ (99 eV) peaks. c) N 1s region of Si silicon wafers after APTES deposition. The N 1s signal components corresponding to free amines (red) and hydrogen bonded/protonated amines (blue) are identified. d) C 1s region of polycrystalline Si wafers after acacPEGA deposition. Different oxidation states are identified: C—C (Red), C—O (Blue), O—C—O/C=O (green) and O—C=O (yellow). e) XPS spectra of the Eu 3d core level in the Si wafers after acacPEGA deposition (black) and after anchoring the $\beta$-ketoester complex (red). f) XPS spectrum of the Tb $3d_{5/2}$ core level in the Si wafers after anchoring the $\beta$-ketoester complex.

Figure 3b shows the temperature-dependent emission spectra (296–338 K) presenting the characteristic narrow lines assigned to the $^5D_4 \rightarrow ^7F_{5,6}$ ($Tb^{3+}$) and the $^5D_0 \rightarrow ^7F_{1\text{-}4}$ transitions ($Eu^{3+}$). There is an overlap between the $^5D_0 \rightarrow ^7F_1$ and the $^5D_4 \rightarrow ^7F_4$ transitions in the wavelength range 570–605 nm. As the temperature increases, we observe a decrease in the integrated emission areas of both ions (Figure 3c). The relative decrease is much more pronounced in the $^5D_4 \rightarrow ^7F_5$ transition (labeled as $I_1$) than in the $^5D_0 \rightarrow ^7F_2$ one (labeled as $I_2$), 38% and 17%, respectively. The energy of the DPA triplet (27050 $cm^{-1}$[42,43]) prevents $^5D_4$-to-ligand and $^5D_0$-to-ligand energy back-transfer, as occurs in other $Tb^{3+}/Eu^{3+}$ molecular thermometers.[26] Moreover, the analysis of the emission spectra recorded at different temperatures in the 296–338 K range reveals absolutely no changes in the first coordination sphere of the lanthanides (Figure S2 in the Supporting Information).

The most remarkable feature of the temperature dependent luminescence, however, is that it depends on the temperature change induced in the surface. Upon heating from 296 to 338 K, the $I_1$ and $I_2$ integrated areas decrease 40% and 15%, respectively, relatively to the values at 296 K. On cooling, when the temperature reaches this later value, the initial intensity value is recovered, although a clear hysteresis is discerned. The repetition of this intensity variation over several heating–cooling cycles shows that the hysteresis is an intrinsic feature of the system and, thus, the monolayer can be consider as a thermometric molecular probe.

The surface temperature of the SAM in the heating or cooling ramp is accessed through the ratiometric thermometric parameter $\Delta = I_1/I_2$, whose evolution with temperature in four consecutive heating–cooling cycles shows essentially the same hysteresis cycle presented by the integrated areas $I_1$ and $I_2$ (**Figure 4**). Noticeable, there is a very good reproducibility (higher than 98.4% after a complete cycle) under temperature cycling. The performance of the molecular thermometer is given by its relative sensitivity, defined as

$$S_r = \frac{1}{\Delta}\frac{\partial \Delta}{\partial T} \quad (1)$$

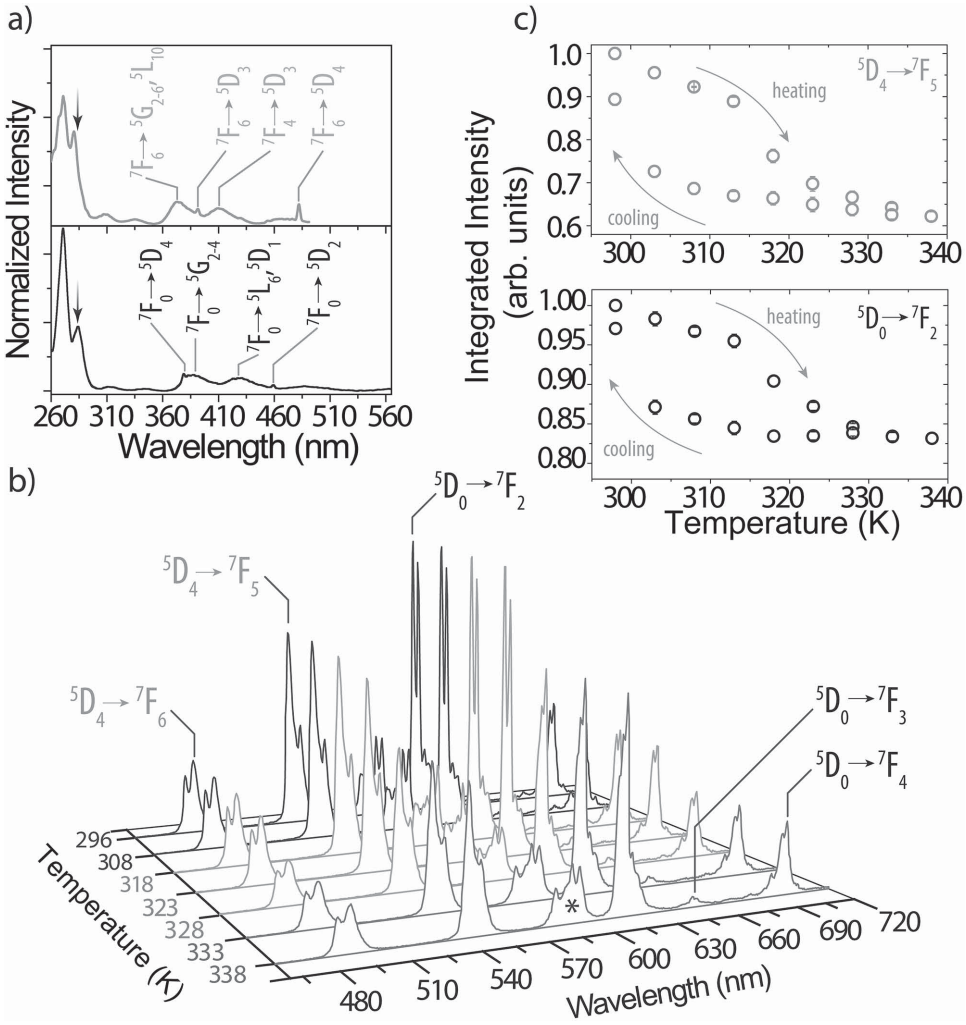


**Figure 3.** a) Excitation spectrum of the functionalized Si surface at 296 K. The top and bottom lines correspond to the monitoring of the $^5D_4 \rightarrow {}^7F_5$ ($Tb^{3+}$) and $^5D_0 \rightarrow {}^7F_2$ ($Eu^{3+}$) transitions, respectively. b) Emission spectra excited at 280 nm (the vertical arrow marked in (a)). The transitions assigned to $Tb^{3+}$ and to $Eu^{3+}$ are presented in gray and black, respectively. The asterisk marks the spectral region where an overlap between the $Tb^{3+}$ transition $^5D_4 \rightarrow {}^7F_4$ and $Eu^{3+}$ transitions $^5D_0 \rightarrow {}^7F_{0,1}$ is observed. c) Normalized integrated area of the $^5D_4 \rightarrow {}^7F_5$ (top) and $^5D_0 \rightarrow {}^7F_2$ (bottom) transitions in a single heating–cooling cycle between 296 and 338 K, computed from the emission spectra under 280 nm excitation.

The present $Ln^{3+}$ functionalized SAM presents two sensitivity regimes: i) *regime 1* corresponding to the lowest sensitivity (around 0.25% $K^{-1}$) and ii) *regime 2* with enhanced in the range 308–323 K reaching a maximum value of 1.43% $K^{-1}$ at 323 K when the temperature is being raised. The corresponding minimum temperature uncertainty computed according the literature conventional procedure[33] is 0.3 K.

Envisaging for any topographic changes on the SAM, we take AFM topography images on the same sample used in the photoluminescence characterization when the temperature increase from 296 to 338 K with steps of 5°, and then after cooling to 296 K (Figure S3 in the Supporting Information). Within the measurement errors no changes were observed in the scanned area and thus we conclude that the temperature variations produce negligible changes in the surface topography. ESEM images taken in the same temperature range are consistent with the observations made by AFM (Figure S4 in the Supporting Information).

Moreover, we recorded XRR patterns of the functionalized Si surface and observed the typical oscillations of thin films with well-defined thickness (**Figure 5**a). Two oscillations are discernable showing the presence of two layers with different densities and thickness. The longer oscillation corresponds to a characteristic thickness of ≈7 nm and can be ascribed to the thermometric monolayer coating, while the shorter one corresponds to a characteristic thickness of ≈400 nm being consistent with the $SiO_2$ layer deposited onto the silicon wafer.

Upon temperature cycling the reflectivity pattern of sample shows significant differences (Figure S5 in the Supporting Information). After exposing the sample to two temperature cycles, the XRR pattern was recorded during a heating cycle. From the oscillations associated to the thermometric monolayer, we compute the layer thickness ($t$) from the scattering vector

$$q = \frac{4\pi}{\lambda}\sin(\omega) \quad (2)$$

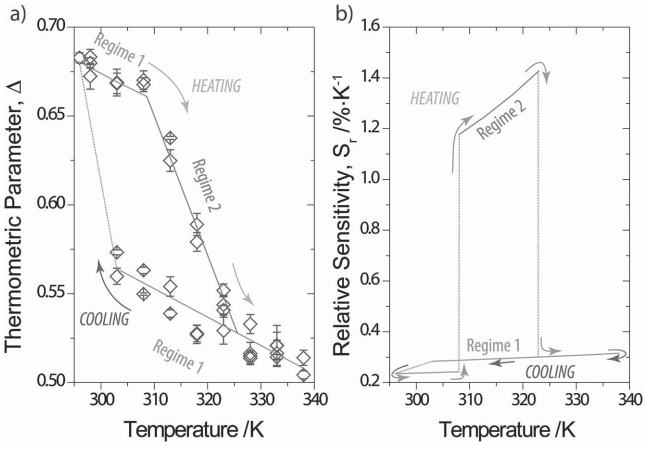


**Figure 4.** a) Evolution of the thermometric parameter Δ with the temperature in the 296–338 K range in four consecutive heating–cooling cycles (symbols). The solid lines are the fit of experimental data to straight lines in two regimes: *regime 1* (low thermal sensitivity, blue line) and *regime 2* (high thermal sensitivity, pink line). The interrupted line is a guide for the eyes. The thermometric parameter was computed from the emission spectra of the functionalized Si surface under 280 nm excitation. The error bars result from the error in the determination of the integrated areas propagated to the determination of the thermometric parameter. b) Sensitivity curve in the 296–338 K range computed from the fitting curves in both regimes. The maximum sensitivity value is 1.43% $K^{-1}$ at 323 K.

where $\lambda$ is the X-ray wavelength and $\omega$ is the diffraction angle. The distance between the first and second fringe minima is the layer thickness, given by $t = 4\pi/\Delta q$. Figure 5c shows that the computed thickness is constant with the increasing of temperature, except in the 306–314 K range where it shows larger values (corresponding to the interval where $\Delta$ changes more dramatically).

## 3. Discussion

The synthetic method used here is simple and follows to some extent the methodology already developed by some of us for the immobilization of biomolecules on Si-based microstructures through the formation of SAMs.[44,45] The process involves surface activation by ozonolisis, vapor coating with APTES, and self-assembling of acacPEGA polymers by the Michael reaction. The characterization of the Si surfaces at every step of the coating procedure shows that all the processes from surface modification with APTES, Michael addition of hydrophilic acacPEGA chains, and docking of luminescent $Tb^{3+}$ and $Eu^{3+}$ complexes to the end of this chain were successful and resulted in the formation of a self-assembled-monolayer on the silicon surface. In general, the coating surface was very homogeneous and smooth, in the scale of AFM observations. The roughness values are consistent with a monolayer thickness. XPS are also consistent with a full covering of the surface at every deposition step as the signal of surface elements, Si, N, was progressively weakened.

The luminescent $Tb^{3+}$ and $Eu^{3+}$ complexes provide thermal functionality to the SAM in the physiological range. In comparison with already reported $Eu^{3+}/Tb^{3+}$ thermometric systems,[26,31,33,43,46] we observe a response that depends on the temperature change induced in the surface. In all of the reported examples, the variation of the thermometric parameter follows a single trend in the whole working temperature range, and this range was quite wide (at least tenths of degrees).[47–50] It is evident that the implementation of the lanthanide complex thermometric system on this family of SAM makes a significant difference in the thermometric process. The smooth decrease in $\Delta$ in the 296–308 K range and above 323 K ( *regime 1*) may be interpreted by a thermally driven back energy transfer from the $Eu^{3+}$ and $Tb^{3+}$ ions to the acacPEGA chains depopulating the corresponding $^5D_4$ and $^5D_0$ emitting states. However, in the 308–323 K range (*regime 2*), we observe a suddenly decrease in $\Delta$ ascribed to a subtle structural transition of the acacPEGA chains detected by XRR analysis as a change of layer thickness, close to the limit of resolution of the technique and undetected by AFM or ESEM inspection. Although the $\Delta$ parameter presents a clear hysteretic cycle, the temperature determination is unequivocal, as a small temperature variation (≈1°) induces completely different changes on $\Delta$ depending in what *regime* (*1* or *2*) the system is (in *regime 1* the signal vary ≈1.3%, whereas in *regime 2* it changes ≈0.3%). Variations in the $\Delta$ parameter of 0.3% are easily measured with commercial portable detectors ($\delta\Delta/\Delta \approx 0.1\%$).

Bistability on luminescent lanthanide-based materials was reported for single (e.g., $Cs_3Y_2Br_9$: $Yb^{3+}$,[51] $YCa_4O(BO_3)_3$: $Yb^{3+}$[52]) and doubly (e.g., $CsCdBr_3$:$Yb^{3+}$,$Er^{3+}$[53]) doped rare earth crystals and also for rare earth crystals doped with rare earth ions (e.g., $NdPO_4$:$Yb^{3+}$[54]). In this last example, for instance, its origin was ascribed to the interplay between $Nd^{3+}\leftrightarrow Yb^{3+}$ energy transfer processes and on the large pump-induced thermal loading characteristic of the $NdPO_4$ host. For excitation intensities ranging from 0.7 to $2.8 \times 10^3$ W $cm^{-2}$, the local temperature of the crystal (temperature at the pumping volume) is raised above 300 K activating $Nd^{3+}\leftarrow Yb^{3+}$ energy back-transfer processes. In the present case, however, the SAM is excited using much lower power densities, $30 \times 10^{-6}$ W $cm^{-2}$ at 280 nm, inducing negligible thermal gradients within the sample. Moreover, as mentioned above, there is no evidence of $Tb^{3+}$-to-$Eu^{3+}$ energy transfer and, thus, the bistability is ascribed to the subtle structural transition of the acacPEGA chain.

Conformational transitions are reported in the literature as responsible for step-like changes in the response of thermometric systems based on polymers.[55] When these polymers are interconnected with optical emitters, such as Au nanoparticles, QDs, and $Ln^{3+}$ phosphors, that temperature dependent-transition can induce changes in the local environment of the emitters producing variations on their absorption/emission features (intensity, energy, or lifetime).[56,57] This is not, however, what we observe here. There is no evidence of thermally driven Tb-to-Eu energy transfer and $^5D_4$,$^5D_0$-to-ligand (DPA) energy back transfer. Moreover, the first coordination sphere of the two lanthanides is unaltered when temperatures increases from 296 to 338 K. Therefore, the observed decrease of the $^5D_4 \rightarrow {}^7F_5$ and $^5D_0 \rightarrow {}^7F_2$ integrated intensities are explained by the activation of nonradiative decay pathways involving the acacPEGA chains. We are able to use the $^5D_4 \rightarrow {}^7F_5/{}^5D_0 \rightarrow {}^7F_2$ integrated intensity ratio to measure the temperature because they are thermally quenched at different rates. In fact, the $Tb^{3+}$ transition is the

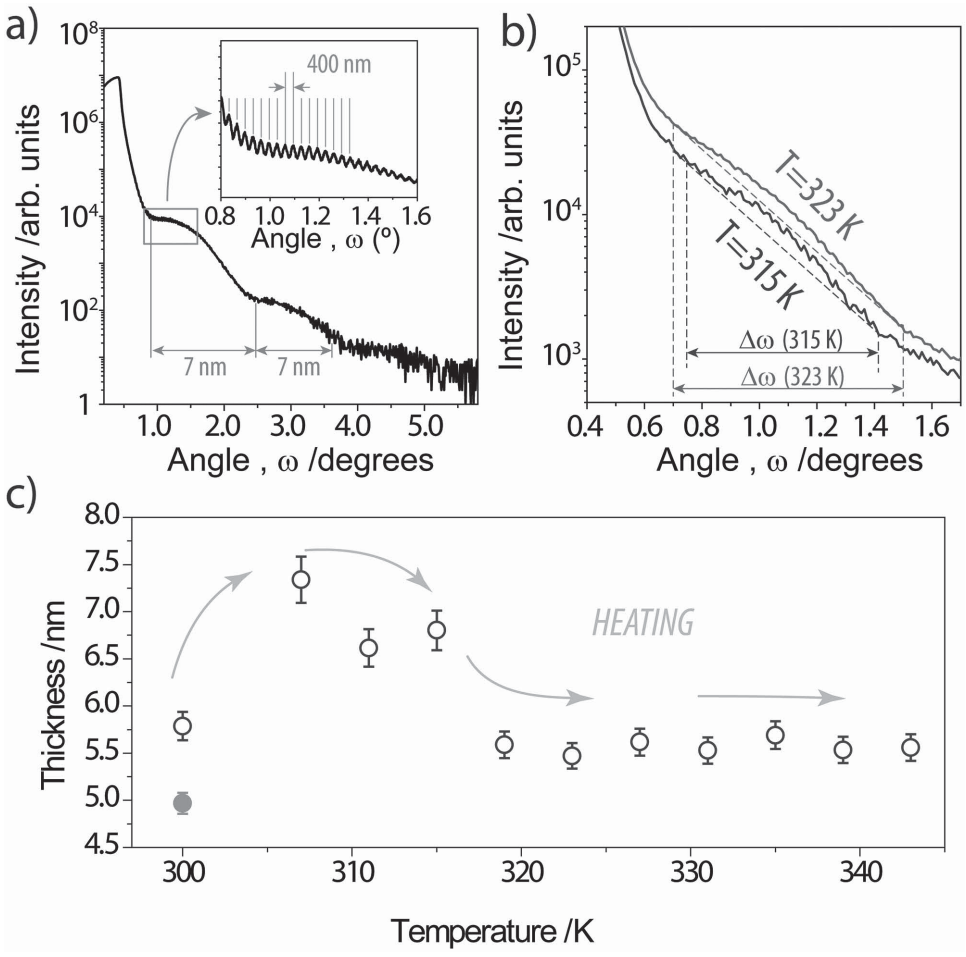


**Figure 5.** a) Room temperature XRR reflectivity pattern of the functionalized Si surface. Inset shows zoom over the region marked in blue. b) XRR pattern of functionalized Si wafer sample obtained at 315 and 323 K, showing a small change in the interfringes spacing. Both patterns were recorded after exposing the sample to five consecutive temperature cycles. c) Temperature dependence of the thermometric monolayer thickness. Open symbols correspond to results obtained at increasing temperatures while the filled symbol denotes the result obtained at room temperature after cooling.

most sensitive to changes in the acacPEGA conformation probably because the thermally induced depopulation is higher for the level ($^5D_4$) presenting higher energy resonance with the excited states of the acacPEGA chains (the $^5D_4$ energy is higher than that of the $^5D_0$ level).

A relevant example describes the transition from hydrophilic-swollen-globule-state to hydrophobic-collapsed-coil-state in PEG-based polymers.[58] On the other hand, photon correlation spectroscopy and Raman scattering experiments of free PEG chains in aqueous solutions heated from 293 to 333 K show an increase of the hydrodynamic size up to 313 K (attributed to chain expansion) and, then, a decrease up to 333 K, (attributed to water loss), in good agreement with the occurrence of a reversible structural transition of the polymer chains, as suggested by the results presented in Figure 5c. Additionally PEG thermosensitive behavior has been observed in nanoparticles of cross-linked ZnO@PEG acrylate hydrogels presenting swelling transitions (determined by dynamic light scattering) in the range 310–315 K[56] (the same range in which we observe the photoluminescence hysteresis, Figure 3c, and the increase of the monolayer thickness, Figure 5c). Thus, both the XRR results (Figure 5) and previous reports on PEG-based chains suggest that the thermometric *regime 2* can be associated with a conformational transition in the acacPEGA chains. However, how is this affecting the structure of the lanthanide complexes at the end of the chain is not entirely understood. The structure of $Eu^{3+}$ and $Tb^{3+}$ complexes of acac and DPA found in their corresponding crystalline compounds is shown in Figure S6 in the Supporting Information. We may assume that, like in the crystals, DPA ligands are almost planar and parallel to the Si surface, and acac is disposed perpendicularly. Comparing acac and DPA areas, it is clear that only a small ratio (1:6) of acacPEGA chains will hold a complex. The shrinking of the PEG chains may cause a change not only on the lanthanide ligand binding distances, but also on the distance with free acac groups, and on the orientation of the light harvesting aromatic rings that would decrease the photon capturing efficiency. Any of these changes would accelerate the decrease of emission intensity with the temperature.

Maybe one of the most noteworthy application of bistable systems is molecular logic where molecules are used to mimic the logical functions usually implemented in

a)

| Entry | Input-1 Excitation (280 nm) | Input-2 $\Delta T>T_c$ | Output-1 Δ(T) in Regime 1 | Output-2 Δ(T) in Regime 2 |
|---|---|---|---|---|
| 1 | 0 | 0 | 0 | 0 |
| 2 | 1 | 0 | 1 (0) | 0 (1) |
| 3 | 0 | 1 | 0 | 0 |
| 4 | 1 | 1 | 0 (1) | 1 (0) |

b)

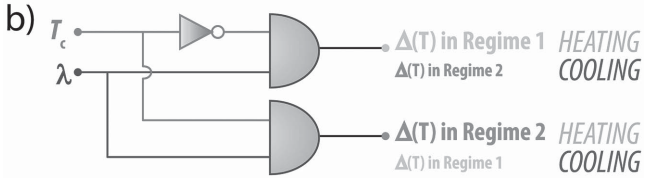


**Figure 6.** a) Truth table for the INHIBIT and AND logic gates on heating (296–338 K) (cooling from 338 to 296 K). *Tc* = 15 or 35° on heating and cooling, respectively (Figure 4a). b) Circuit diagram and c) schematic switching operation of the 1:2 molecular DEMUX logic device.

semiconductor-based technology.[59,60] Contrary to the well-implemented electronic devices, molecular logic systems permits full integration with biological entities, such as cells, and when, as in the present SAM, the output signal emerges as fluorescence light, which can be detected without contact with the probe, the logical systems gain special interest. The $Ln^{3+}$-based SAM can be used for the construction of optically active molecular logic gates with INHIBIT and AND logic functions, depending on two physical inputs, excitation wavelength and heat transferred to the system on heating from 296 K (or heat transferred from the system, on cooling from 338 K), **Figure 6**. In the absence of both inputs no emission signal as output is observed, thus, both output-1—Δ(*T*) calibration curve in *regime 1*—and output-2—Δ(*T*) calibration curve in *regime 2*—become "0" (entry 1). When a particular excitation wavelength is used as input-1, the $^5D_4 \rightarrow {}^7F_5$ and $^5D_0 \rightarrow {}^7F_2$ transitions are discerned; thus, output-1 becomes "1" ("0" on cooling) and output-2 becomes "0" ("1" on cooling) (entry 2). When the SAM is heated (or cooled),as input-2, and no excitation wavelength is used, no emission signals are observed; thus, both output-1 and output-2 become "0" (entry 3). However, in the presence of both inputs, Δ(*T*) follows the calibration curve of *regime 2* (of *regime 1* on cooling), which is defined as output-2, which becomes "1" ("0" on cooling); meanwhile, output-1 is "0" ("1" on cooling) (entry 4), Figure 6a. Accordingly, the truth table value for output-1 forms an INHIBIT logic gate (a AND gate on cooling), whereas the value of output-2 forms a AND logic gate (an INHIBIT gate on cooling).[60] The $Ln^{3+}$-based SAM is a two-module molecular demultiplexer (DEMUX)[61] where the output is switched between the Δ(*T*) calibration curve in *regime 1* and that in *regime 2*, with light at 280 nm as the input and the heat transferred to the system (on heating) (or transferred from the system, on cooling) as the control, Figure 6b. This is one more example of molecular logic gates using $Ln^{3+}$ ions[62–64] but the first case in which a molecular thermometer can operate as a double-input logic element in the 296–338 K range. Furthermore, this is one of the rare examples of a molecular logic device that depends on physical inputs rather than chemical ones, as previously reported, permitting a faster switching speed.

## 4. Conclusions

The first self-assembled polymer monolayer encompassing complexes of trivalent lanthanide ions producing a ratiometric temperature readout were fabricated on Si surfaces. All the functionalization steps were described and a complete characterization of the surface constitution, morphology, and topography was made. The monolayer demonstrate competitive thermal sensitivity (1.43% $K^{-1}$) and low temperature readout uncertainty (0.3 K) combined with high repeatability (98.6%). The system is characterized by a dual-sensitive regime resulting from the hysteresis of its photoluminescence. We rationalize the observations based a reversible structural transition of the polymer chains that confers a large enhancement of the thermometer sensitivity in a small temperature range. Manifestly, the $Ln^{3+}$ system originally designed to give a ratiometric temperature readout is a molecular probe able to discern a phase transition in the acacPEGA chain, being thus the most acute probe of that transition among those used by us, namely, ESEM, AFM, XPS, and XRR. The temperature reading can be quite straightforward opening the possibility to be implemented using conventional optical fibers and portable detectors, or by using of a charge coupled device (CCD) camera to map the sample's surface temperature with spatial resolution limited only by the optical detection system. One can foresee potential applications of such functionalized surfaces phase transitions probing, particularly that occurring at the nanoscale, where traditional calorimetric techniques are not useful due to the limited amount of material, microscope-based techniques may overlook the transitions and reflectometry techniques may also be of limited applicability due to the relatively poor ordering of the thin films. In this context, emission of the lanthanide complexes give a clear signature of the phase transition and may further be explored as an order parameter representing the transition with indications about its dynamics, for instance. Moreover, the observed reversible bistability permits that the silicon-functionalized surface can operate as an optically active two-module molecular DEMUX opening the possibility of use this computing molecule in medical- and biotechnologies, such as blood diagnostics, "lab-on-a-molecule" systems, and molecular computational identification of small objects.[60] Future work will also contemplate the influence of distinct heating–cooling ramps on the response of the system to test the frequency range limits where the logic gates operate.

## 5. Experimental Section

*Materials*: Europium(III) chloride hexahydrate ($EuCl_3$ $(H_2O)_6$, 99.9%), terbium(III) chloride hexahydrate ($TbCl_3$ $(H_2O)_6$, 99.9%), 2,6-pyridinedicarboxylic acid (DPA, 99%) (3-aminopropyl)triethoxysilane (APTES), Poly(ethylene glycol) (PEG, Mn: 200 Da), triethylamine, acryloyl chloride (97%), anhydrous sodium acetate (NaOAc, 95%), and 2,2,6-trimethyl-*4H*-1,3-dioxin-4-one were purchased from Aldrich and used as received. Polyethylene glycol acrylate (PEGA) was synthesized and purified by improving an extraction/fractionation method previously

described by Klier et al.[65] and Ali et al.[66] The $\beta$-ketoester polyethylene glycol derivative (acacPEGA) was synthesized by adapting the method describe by Shridharan et al.[67]

*Methods—NMR and FT–IR*: The $^1$H NMR spectra were recorded at 400 MHz in $CDCl_3$ solution at room temperature using a Bruker AV-400 spectrometer. The $^1$H NMR spectra were fully consistent with their chemical structures and confirmed the purity of the final compounds. FT–IR spectra were recorded at room temperature in a Perkin Elmer Spectrum 100 FT-IR spectrometer equipped with a Universal ATR sampling accessory with 4 $cm^{-1}$ resolution within 380–4000 $cm^{-1}$ region. Purity of the polyethylene glycol derivatives was additionally checked by mass spectrometry (MALDI TOF-MS) using dithranol (DTH) as matrix and sodium trifluoroacetate as cationization agent in a Bruker MicroFlex spectrometer.

*Surface Characterization*: Contact angle experiments were performed using a contact angle goniometer (THETALITE100 with the software One Attention, Finland). Values of the contact angle on at least three samples were measured to give statistical significance. Atomic force microscopy (AFM) and environmental scanning electron microscopy (ESEM) were carried out, respectively, in a Ntegra Aura (NT-MDT) equipment and in a ESEM Quanta FEG 250 microscope equipped with a Peltier heating/cooling system. The X-ray photoelectron spectroscopy (XPS) analysis was carried out using a Kratos Axis Ultra spectrometer employing a monochromatic Al K$\alpha$ (1486,6 eV)10 mA, 15 kV) X-ray source and a power of 150 W.

*X-Ray Reflectivity*: The X-ray reflectivity (XRR) patterns were performed on a Philips X'Pert MRD using monochromatic Cu K$\alpha$ radiation ($\lambda$ = 1.541 Å) in the $0.2 < \theta < 5$ ° range (0.01° resolution). The incident beam optics included a divergence slit (Crossed Slit Collimator) and the reflected beam optics included a Soller slit of 2.29° and a parallel Plate Collimator (0.27° opening). Sample was aligned at each temperature using standard procedures.[68] Heating was achieved using a IES-RD31 temperature controller and a Peltier unit.

*Photoluminescence and Temperature Control*: The photoluminescence spectra were recorded with a modular double grating excitation spectrofluorimeter with a TRIAX 320 emission monochromator (Fluorolog-3, Horiba Scientific) coupled to a R928 Hamamatsu photomultiplier, using a front face acquisition mode. The excitation source was a 450 W Xe arc lamp. The emission spectra were corrected for detection and optical spectral response of the spectrofluorimeter and the excitation spectra were corrected for the spectral distribution of the lamp intensity using a photodiode reference detector. The temperature was controlled using an IES-RD31 controller and a Kapton thermofoil heater from Minco mounted on a copper holder and monitored using a thermo-couple thermometer Barnant 100 (model 600-2820) with a temperature accuracy of 0.1 K, accordingly to the manufacturer. The temperature ramp in the heating–cooling cycles is 1° $min^{-1}$.

## Supporting Information

Supporting Information is available from the Wiley Online Library or from the author.

## Acknowledgements

Financial support from the Spanish Ministry of Science and Innovation research grants BFU2009-12763/BFI, MAT2011-259911, TEC2011-29140, and TEC2014-51940, and Project Consolider-Ingenio in Molecular Nanoscience CSD2007-00010 are gratefully acknowledged. Moreover, the work was partially developed in the scope of the project CICECO – Aveiro Institute of Materials (Ref. FCT UID/CTM/50011/2013), financed by Portuguese funds through the FCT/MEC and when applicable cofinanced by FEDER under the PT2020 Partnership Agreement. C.D.S.B. and N.J.O.S. thank the Portuguese Fundação para a Ciência e Tecnologia (FCT) for their grants (SFRH/BPD/89003/2012 and IF/01653/2013, respectively). The authors acknowledge Rosario Soares (Aveiro) and M. Tomas (Zaragoza) for support in the XRR and helpful discussions, respectively.

Received: September 14, 2015
Revised: October 22, 2015
Published online: November 30, 2015

[1] E. Southern, K. Mir, M. Shchepinov, *Nat. Genet.* **1999**, *21*, 5.
[2] S. F. Bent, *Surf. Sci.* **2002**, *500*, 879.
[3] S. Onclin, B. J. Ravoo, D. N. Reinhoudt, *Angew. Chem. Int. Ed.* **2005**, *44*, 6282.
[4] T. L. Zhou, R. T. Anderson, H. S. Li, J. Bell, Y. A. Yang, B. P. Gorman, S. Pylypenko, M. T. Lusk, A. Sellinger, *Nano Lett.* **2015**, *15*, 3657.
[5] F. F. Tao, S. Bernasek, *Functionalization of Semiconductor Surfaces*, John Wiley & Sons, Inc., New York **2012**.
[6] *Temperature Sensors Market Analysis By Application (Automotive, Consumer Electronics, Environmental, Medical, Process Industries) and Segment Forecasts to 2020*, Grand View Research, San Francisco, CA, USA **2015**.
[7] G. Eranna, *Crystal Growth and Evaluation of Silicon for VLSI and ULSI*, CRC Press, Boca Raton, FL, USA **2015**.
[8] S. A. Campbell, *The Science and Engineering of Microelectronic Fabrication*, Oxford University Press, New York **2001**.
[9] X. Perpiña, X. Jordà, N. Mestres, M. Vellvehi, P. Godignon, J. Millan, H. von Kiedrowski, *Meas. Sci. Technol.* **2004**, *15*, 1011.
[10] L. Shi, C. Dames, J. R. Lukes, P. Reddy, J. Duda, D. G. Cahill, J. Lee, A. Marconnet, K. E. Goodson, J. H. Bahk, A. Shakouri, R. S. Prasher, J. Felts, W. P. King, B. Han, J. C. Bischof, *Nanoscale Microscale Thermophys. Eng.* **2015**, *19*, 127.
[11] M. Mecklenburg, W. A. Hubbard, E. R. White, R. Dhall, S. B. Cronin, S. Aloni, B. C. Regan, *Science* **2015**, *347*, 629.
[12] L. S. Jang, H. J. Liu, *Biomed. Microdevices* **2009**, *11*, 331.
[13] R. C. Webb, A. P. Bonifas, A. Behnaz, Y. H. Zhang, K. J. Yu, H. Y. Cheng, M. X. Shi, Z. G. Bian, Z. J. Liu, Y. S. Kim, W. H. Yeo, J. S. Park, J. Z. Song, Y. H. Li, Y. G. Huang, A. M. Gorbach, J. A. Rogers, *Nat. Mater.* **2013**, *12*, 938.
[14] R. A. S. Ferreira, C. D. S. Brites, C. M. S. Vicente, P. P. Lima, A. R. N. Bastos, P. G. Marques, M. Hiltunen, L. D. Carlos, P. S. André, *Laser Photon. Rev.* **2013**, *7*, 1027.
[15] A. Benayas, B. del Rosal, A. Perez-Delgado, K. Santacruz-Gomez, D. Jaque, G. A. Hirata, F. Vetrone, *Adv. Opt. Mater.* **2015**, *3*, 687.
[16] J. Millán, P. Godignon, X. Perpiña, A. Perez-Tomas, J. Rebollo, *IEEE Trans. Power Electron.* **2014**, *29*, 2155.
[17] C. D. S. Brites, P. P. Lima, N. J. O. Silva, A. Millán, V. S. Amaral, F. Palacio, L. D. Carlos, *Nanoscale* **2012**, *4*, 4799.
[18] D. Jaque, F. Vetrone, *Nanoscale* **2012**, *4*, 4301.
[19] X. D. Wang, O. S. Wolfbeis, R. J. Meier, *Chem. Soc. Rev.* **2013**, *42*, 7834.
[20] K. Okabe, N. Inada, C. Gota, Y. Harada, T. Funatsu, S. Uchiyama, *Nat. Commun.* **2012**, *3*, 705.
[21] L. M. Maestro, Q. Zhang, X. Li, D. Jaque, M. Gu, *Appl. Phys. Lett.* **2014**, *105*, 181110.
[22] S. J. Cho, D. Maysinger, M. Jain, B. Roder, S. Hackbarth, F. M. Winnik, *Langmuir* **2007**, *23*, 1974.
[23] A. Gnach, T. Lipinski, A. Bednarkiewicz, J. Rybka, J. A. Capobianco, *Chem. Soc. Rev.* **2015**, *44*, 1561.
[24] J. C. G. Bünzli, S. V. Eliseeva, *Chem. Sci.* **2013**, *4*, 1939.
[25] L. D. Carlos, R. A. S. Ferreira, V. de Zea Bermudez, S. J. L. Ribeiro, *Adv. Mater.* **2009**, *21*, 509.
[26] C. D. S. Brites, P. P. Lima, N. J. O. Silva, A. Millán, V. S. Amaral, F. Palacio, L. D. Carlos, *Adv. Mater.* **2010**, *22*, 4499.

[27] H. Peng, M. I. Stich, J. Yu, L. N. Sun, L. H. Fischer, O. S. Wolfbeis, *Adv. Mater.* **2010**, *22*, 716.
[28] Y. Cui, H. Xu, Y. Yue, Z. Guo, J. Yu, Z. Chen, J. Gao, Y. Yang, G. Qian, B. Chen, *J. Am. Chem. Soc.* **2012**, *134*, 3979.
[29] U. Rocha, C. Jacinto da Silva, W. Ferreira Silva, I. Guedes, A. Benayas, L. Martínez Maestro, M. Acosta Elias, E. Bovero, F. C. van Veggel, J. A. García Solé, D. Jaque, *ACS Nano* **2013**, *7*, 1188.
[30] V. Lojpur, G. Nikolic, M. D. Dramicanin, *J. Appl. Phys.* **2014**, *115*, 203106.
[31] R. Piñol, C. D. Brites, R. Bustamante, A. Martínez, N. J. Silva, J. L. Murillo, R. Cases, J. Carrey, C. Estepa, C. Sosa, F. Palacio, L. D. Carlos, A. Millán, *ACS Nano* **2015**, *9*, 3134.
[32] E. Hemmer, M. Quintanilla, F. Legare, F. Vetrone, *Chem. Mater.* **2015**, *27*, 235.
[33] Z. P. Wang, D. Ananias, A. Carne-Sanchez, C. D. S. Brites, I. Imaz, D. Maspoch, J. Rocha, L. D. Carlos, *Adv. Funct. Mater.* **2015**, *25*, 2824.
[34] C. D. S. Brites, P. P. Lima, N. J. O. Silva, A. Millán, V. S. Amaral, F. Palacio, L. D. Carlos, *New J. Chem.* **2011**, *35*, 1177.
[35] C. D. S. Brites, P. P. Lima, N. J. O. Silva, A. Millán, V. S. Amaral, F. Palacio, L. D. Carlos, *Nanoscale* **2013**, *5*, 7572.
[36] B. D. Mather, K. Viswanathan, K. M. Miller, T. E. Long, *Prog. Polym. Sci.* **2006**, *31*, 487.
[37] T. L. Miller, S. I. Senkfor, *Anal. Chem.* **1982**, *54*, 2022.
[38] K. Binnemans, *Handbook on the Physics and Chemistry of Rare Earths*, Vol. *35* (Eds: K. A. Gschneidner Jr., J.-C. G. Bünzli, V. K. Pecharsky), Elsevier, Amsterdam **2005**, p. 107.
[39] J. A. Howarter, J. P. Youngblood, *Langmuir* **2006**, *22*, 11142.
[40] F. Mercier, C. Alliot, L. Bion, N. Thromat, P. Toulhoat, *J. Electron. Spectrosc.* **2006**, *150*, 21.
[41] S. Maji, S. Kumar, K. Sankaran, *Spectrochim. Acta A* **2015**, *135*, 405.
[42] M. Latva, H. Takalo, V. M. Mukkala, C. Matachescu, J. C. Rodriguez-Ubis, J. Kankare, *J. Lumin.* **1997**, *75*, 149.
[43] C. D. S. Brites, P. P. Lima, L. D. Carlos, *J. Lumin.* **2015**, DOI: 10.1016/j.jlumin.2015.01.025.
[44] O. Penon, D. Siapkas, S. Novo, S. Duran, G. Oncins, A. Errachid, L. Barrios, C. Nogues, M. Duch, J. A. Plaza, L. Perez-Garcia, *Colloids Surf. B* **2014**, *116*, 104.
[45] O. Penon, S. Novo, S. Duran, E. Ibanez, C. Nogues, J. Samitier, M. Duch, J. A. Plaza, L. Perez-Garcia, *Bioconjugate Chem.* **2012**, *23*, 2392.
[46] C. D. S. Brites, P. P. Lima, N. J. O. Silva, A. Millán, V. S. Amaral, F. Palacio, L. D. Carlos, *J. Lumin.* **2013**, *133*, 230.
[47] S. L. Shinde, K. K. Nanda, *Angew. Chem. Int. Ed.* **2013**, *52*, 11325.
[48] Z. X. Gan, X. L. Wu, J. L. Zhang, X. B. Zhu, P. K. Chu, *Biomacromolecules* **2013**, *14*, 2112.
[49] H. Huang, H. Li, A. J. Wang, S. X. Zhong, K. M. Fang, J. J. Feng, *Analyst* **2014**, *139*, 6536.
[50] J. H. Wang, M. Li, J. Zheng, X. C. Huang, D. Li, *Chem. Commun.* **2014**, *50*, 9115.
[51] M. P. Hehlen, H. U. Gudel, Q. Shu, J. Rai, S. Rai, S. C. Rand, *Phys. Rev. Lett.* **1994**, *73*, 1103.
[52] P. Goldner, O. Guillot-Noel, P. Higel, *Opt. Mater.* **2004**, *26*, 281.
[53] S. M. Redmond, S. C. Rand, *Opt. Lett.* **2003**, *28*, 173.
[54] A. Ródenas, D. Jaque, J. G. Solé, A. Speghini, M. Bettinelli, E. Cavalli, *Phys. Rev. B* **2006**, 74.
[55] L. D. Carlos, V. de Zea Bermudez, V. S. Amaral, S. C. Nunes, N. J. O. Silva, R. A. S. Ferreira, J. Rocha, C. V. Santilli, D. Ostrovskii, *Adv. Mater.* **2007**, *19*, 341.
[56] W. T. Wu, J. Shen, P. Banerjee, S. Q. Zhou, *Adv. Funct. Mater.* **2011**, *21*, 2830.
[57] J. Li, X. Hong, Y. Liu, D. Li, Y. W. Wang, J. H. Li, Y. B. Bai, T. J. Li, *Adv. Mater.* **2005**, *17*, 163.
[58] C. Branca, A. Faraone, S. Magazu, G. Maisano, P. Migliardo, V. Villari, *J. Mol. Struct.* **1999**, *482*, 503.
[59] A. P. de Silva, S. Uchiyama, *Nat. Nanotechnol.* **2007**, *2*, 399.
[60] A. P. de Silva, *Chem. - Asian J.* **2011**, *6*, 750.
[61] S. Erbas-Cakmak, O. A. Bozdemir, Y. Cakmak, E. U. Akkaya, *Chem. Sci.* **2013**, *4*, 858.
[62] T. Gunnlaugsson, D. A. Mac Donail, D. Parker, *Chem. Commun.* **2000**, 93.
[63] M. de Sousa, M. Kluciar, S. Abad, M. A. Miranda, B. de Castro, U. Pischel, *Photochem. Photobiol. Sci.* **2004**, *3*, 639.
[64] Y. W. Wang, S. B. Liu, Y. L. Yang, P. Z. Wang, A. J. Zhang, Y. Peng, *ACS Appl. Mater. Interfaces* **2015**, *7*, 4415.
[65] J. Klier, A. B. Scranton, N. A. Peppas, *Macromolecules* **1990**, *23*, 4944.
[66] M. M. Ali, H. D. H. Stöver, *Macromolecules* **2004**, *37*, 5219.
[67] V. Sridharan, M. Ruiz, J. C. Menéndez, *Synthesis* **2010**, *6*, 1053.
[68] P. F. Fewster, *J. Appl. Crystallogr.* **1985**, *18*, 334.